Stellar ^{36,38}Ar$(n,\gamma)^{37,39}$Ar Reactions and Their Effect on Light Neutron-Rich Nuclide Synthesis

M. Tessler,[1] M. Paul,[1,*] S. Halfon,[2] B. S. Meyer,[3] R. Pardo,[4] R. Purtschert,[5] K. E. Rehm,[4] R. Scott,[4] M. Weigand,[6] L. Weissman,[2] S. Almaraz-Calderon,[4] M. L. Avila,[4] D. Baggenstos,[5] P. Collon,[7] N. Hazenshprung,[2] Y. Kashiv,[7] D. Kijel,[2] A. Kreisel,[2] R. Reifarth,[6] D. Santiago-Gonzalez,[4,8] A. Shor,[2] I. Silverman,[2] R. Talwar,[4] D. Veltum,[6] and R. Vondrasek[4]

[1]*Racah Institute of Physics, Hebrew University, Jerusalem 91904, Israel*
[2]*Soreq NRC, Yavne 81800, Israel*
[3]*Department of Physics and Astronomy, Clemson University, Clemson, South Carolina 29634, USA*
[4]*Argonne National Laboratory, Argonne, Illinois 60439, USA*
[5]*Physics Institute, University of Bern, 3012 Bern, Switzerland*
[6]*Goethe University Frankfurt, Frankfurt 60438, Germany*
[7]*Department of Physics, University of Notre Dame, Notre Dame, Indiana 46556, USA*
[8]*Department of Physics and Astronomy, Louisiana State University, Baton Rouge, Louisiana 70803, USA*

(Received 5 February 2018; revised manuscript received 24 July 2018; published 11 September 2018)

The ^{36}Ar$(n,\gamma)^{37}$Ar ($t_{1/2} = 35$ d) and ^{38}Ar$(n,\gamma)^{39}$Ar (269 yr) reactions were studied for the first time with a quasi-Maxwellian ($kT \sim 47$ keV) neutron flux for Maxwellian average cross section (MACS) measurements at stellar energies. Gas samples were irradiated at the high-intensity Soreq applied research accelerator facility-liquid-lithium target neutron source and the ^{37}Ar/^{36}Ar and ^{39}Ar/^{38}Ar ratios in the activated samples were determined by accelerator mass spectrometry at the ATLAS facility (Argonne National Laboratory). The ^{37}Ar activity was also measured by low-level counting at the University of Bern. Experimental MACS of ^{36}Ar and ^{38}Ar, corrected to the standard 30 keV thermal energy, are 1.9(3) and 1.3(2) mb, respectively, differing from the theoretical and evaluated values published to date by up to an order of magnitude. The neutron-capture cross sections of ^{36,38}Ar are relevant to the stellar nucleosynthesis of light neutron-rich nuclides; the two experimental values are shown to affect the calculated mass fraction of nuclides in the region $A = 36$–48 during the weak s process. The new production cross sections have implications also for the use of ^{37}Ar and ^{39}Ar as environmental tracers in the atmosphere and hydrosphere.

DOI: 10.1103/PhysRevLett.121.112701

The argon isotopes ^{36}Ar and ^{38}Ar are among the rare stable nuclides for which no experimental neutron-capture cross sections exist above thermal energy. While the abundances of ^{36,38}Ar in terrestrial atmospheric argon are very low relative to ^{40}Ar (produced mainly from ^{40}K decay [1,2]), ^{36}Ar (84.59%) and ^{38}Ar (15.38%) are the major argon isotopes in the solar system [3] and likely so in stellar matter. They are expected, together with the branching point ^{39}Ar, to play a role in nucleosynthesis of light neutron-rich nuclei (e.g., ^{36}S, ^{40}Ar, ^{40}K), believed to be produced during the weak s-process phase of stellar evolution [4,5]. The ^{40}K ($t_{1/2} = 1.248(3)$ Gy [6]) nuclide, in particular, is an important cosmo- or geochronometer and was used to estimate the age and duration of the s process as ~10 Gy [7,8]. ^{40}K can be produced also in explosive oxygen burning [9] as a primary nucleosynthesis product in a massive star of initially pure hydrogen, while the (secondary) s-process production of ^{40}K requires initial abundances of heavy species. A better understanding of Ar cross sections will help clarify the relative primary vs secondary production of ^{40}K. In a different realm of study, the half-life of ^{37}Ar ($t_{1/2} = 35.011(19)$ d [10]) makes this isotope an ideal chronometer for studying circulation and mixing [11], and that of ^{39}Ar (269(3) yr [12]) for dating groundwater [13,14] and ocean water up to about 1000 yr [15]. The atmospheric steady-state concentrations of ^{37}Ar and ^{39}Ar are mainly determined by the spallation reactions ^{40}Ar$(n,4n)^{37}$Ar and ^{40}Ar$(n,2n)^{39}$Ar and at lower neutron energies by the ^{36}Ar$(n,\gamma)^{37}$Ar and ^{38}Ar$(n,\gamma)^{39}$Ar reactions [11]. The latter are also relevant for the estimation of anthropogenic emissions from nuclear installations or for nuclear explosion monitoring [16].

We measured the ^{36}Ar and ^{38}Ar neutron-capture cross sections by activation with quasi-Maxwellian neutrons produced by the ^{7}Li(p,n) reaction at the superconducting linear accelerator of Soreq applied research accelerator facility (SARAF) [17,18] and the liquid-lithium target (LiLiT) [19,20]. The activation products ^{37}Ar and ^{39}Ar were counted off-line by accelerator mass spectrometry (AMS); ^{37}Ar production was also determined by low-level counting (LLC). Neutron irradiation of separate ^{36}Ar and ^{38}Ar samples was performed at the pneumatic transfer tube (rabbit) of the Soreq IRR-1 nuclear reactor in order to remeasure the respective thermal neutron-capture cross

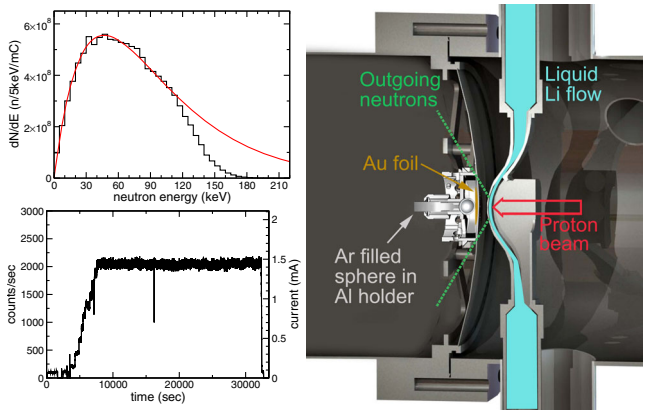

FIG. 1. (Right) Diagram of the LiLiT and activation target assembly. The (∼1.5 mA, ∼9 mm full width) proton beam (open red arrow) impinges on the free-surface lithium film (cyan) (see [19] for details). The Ar-filled sphere and Au foil are positioned in the outgoing neutron cone (green dotted lines) in a vacuum chamber separated from the LiLiT chamber. (Top left) Simulated neutron spectrum incident on the ^{36}Ar sample (black) and a fit in the range $E_n \sim 0$–110 keV with a Maxwell-Boltzmann flux (red) at $kT \sim 47$ keV. (Bottom left) Count rate (left y axis) of fission chamber (see text) and calibration to proton current (right y axis) during the ^{36}Ar run.

sections. Preliminary results of these experiments were reported in [21,22].

Enriched ^{36}Ar, ^{38}Ar, and mixed $^{38}\mathrm{Ar} + {}^{\mathrm{nat}}\mathrm{Ar}$ gas samples were filled into Ti spheres (10 mm outer diameter, 0.2 mm thick Ti shell) [23]. Because of the thermodynamical properties of Ar, the filling was made by successive compression with a custom-made piston and cryogenic pumping in order to achieve the required pressure (∼30 bar). The samples used are listed in Table I. For the samples irradiated at SARAF-LiLiT (Table I), each gas sphere was placed with a 25 mm diameter Au foil (12.5 μm thick), used as a neutron fluence monitor in an evacuated chamber downstream of LiLiT (Fig. 1). LiLiT consists of a windowless film of liquid lithium (1.5 mm thick, 18 mm wide) flowing at 2–3 m/s, serving as both the neutron-producing target and the kilowatt-power beam dump for the incident ∼1.5 mA proton beam [19,20]. The distance from the neutron source to the center of the Ar-filled sphere was 11.3 mm, intercepting ∼30% of the outgoing neutrons. The proton beam energy, measured by Rutherford backscattering off a Au target after the acceleration module, was found to be $1932 \pm 3\,(1940 \pm 3)$ keV for the ^{36}Ar (^{38}Ar) irradiation. A proton beam energy spread of ∼15 keV, estimated from beam dynamics calculations, was verified experimentally [24]. Autoradiographic scans [25] of the Au foils were conducted to determine proton beam centering. An offset of 2.0 (2.2) mm for the ^{36}Ar (^{38}Ar) irradiation was found; this offset was accounted for in our simulations. The neutron yield was continuously monitored with a fission-product ionization chamber [26], located ∼80 cm downstream of the target at 0°. The fission chamber count rate was calibrated to beam current (at low intensity) using a Faraday cup located ∼1 m upstream of the Li target. The total integrated current was ∼10.8(7.35) mA h for the ^{36}Ar (^{38}Ar) irradiation (Fig. 1).

TABLE I. Samples used and the results of the $^{A+1}\mathrm{Ar}/^{A}\mathrm{Ar}$ ratios. ^{36}Ar and ^{38}Ar gas samples [27] were enriched to 99.935% and 99.957% for the respective isotopes. The final $^{37}\mathrm{Ar}/^{36}\mathrm{Ar}$ ratios were obtained by taking a weighted average of the AMS and LLC results (Fig. 2). Sphere no. 52a was irradiated with 1 mm thick Cd shield to estimate the epithermal neutron fraction. The $^{38}\mathrm{Ar}/^{\mathrm{nat}}\mathrm{Ar}$ ratio for sphere 54 (52b) is 11.7 (10.2). For more details see the Supplemental Material [28].

Sphere no.	^{A}Ar (mg)	$^{A+1}\mathrm{Ar}/^{A}\mathrm{Ar}$ ratio
39 (LiLiT)	^{36}Ar (24.5)	$8.6(6) \times 10^{-13}$
52a (reactor, Cd)	^{36}Ar (19.9)	$1.4(1) \times 10^{-12}$
60 (reactor)	^{36}Ar (22.6)	$3.3(2) \times 10^{-10}$
59 (LiLiT)	^{38}Ar (19.5)	$4.0(4) \times 10^{-13}$
54 (reactor)	$^{38,\mathrm{nat}}$Ar (12.8)	$8.6(9) \times 10^{-11}$
52b (reactor)	$^{38,\mathrm{nat}}$Ar (15.8)	$1.8(2) \times 10^{-11}$

The ^{37}Ar nuclide decays by pure electron capture with no γ-ray emission; ^{37}Ar is notable for its role in Davis' solar neutrino experiment [29] where its production via $^{37}\mathrm{Cl}(\nu_e, e^-)^{37}\mathrm{Ar}$ was detected by Auger electron counting. We detected and counted for the first time ^{37}Ar by AMS at the ATLAS facility of Argonne National Laboratory to measure the $^{37}\mathrm{Ar}/^{36}\mathrm{Ar}$ ratio of the irradiated samples. Ar gas was directly fed from the sphere container into an electron cyclotron resonance (ECR) ion source through a remote-controlled sapphire leak valve. $^{36,37}\mathrm{Ar}^{8+}$ ions were extracted from the ion source and accelerated alternately through ATLAS at an energy of 6 MeV/u by appropriate scaling of all accelerator elements. It was found necessary to strip the $^{37}\mathrm{Ar}^{8+}$ ions and count $^{37}\mathrm{Ar}^{18+}$ (fully stripped) in order to suppress the ^{37}Cl ($Z = 17$) background. Stripping was done with a 200 μg/cm^2 C foil at an intermediate stage of the ATLAS linear accelerator. The stripping process (normally not used in AMS measurements at ATLAS), however, produced an isotope fractionation and the effective beam transmission efficiency $[1.84(18) \times 10^{-2}]$ was determined by interpolation between the measured ^{36}Ar and ^{38}Ar transmissions. The $^{37}\mathrm{Ar}^{18+}$ ions were counted using a ΔE-E telescope of Si detectors, 50 and 300 μm thick, respectively, showing background-free spectra; the detection sensitivity in the present experiment was $^{37}\mathrm{Ar}/\mathrm{Ar} \sim 10^{-15}$ (see Supplemental Material [28]).

The ^{37}Ar activity of the same samples was also determined by ultra-LLC in a second stage. Stainless steel vials containing ∼1 cm^3 aliquots of the same activated samples were shipped to the University of Bern. Each gas was quantitatively transferred into a 100 cm^3 copper proportional counter, which was then filled with P6 gas

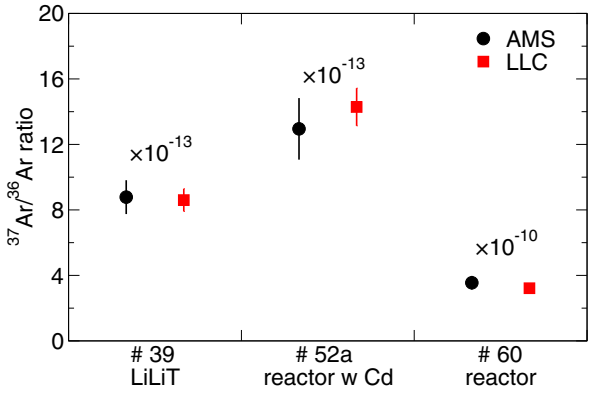

FIG. 2. Comparison of the ^{37}Ar/^{36}Ar ratio (at the end of irradiation) measured by AMS (black) and LLC (red).

(6% methane + 94% commercial ^{37}Ar-free argon) to a pressure of ~6 bar. The ^{37}Ar activity was measured by detecting Auger electrons in an underground LLC laboratory during 1–2 days [16,30]. Energy calibration was performed with copper K-shell x rays ($E = 8.133$ keV) induced by an external ^{241}Am γ source. The ^{37}Ar peak was identified at the K-capture decay energy of 2.82 keV [31] and integrated by means of a Gaussian fit [28]. The amount of ^{36}Ar in the sample was determined, after ^{37}Ar counting, from the filling pressure of the detector and the ^{40}Ar/^{36}Ar ratio measured by mass spectrometry [32] using established procedures. The overall uncertainty of 8% of the final ^{37}Ar/^{36}Ar ratio is dominated by counting statistics and the uncertainties of counting yield (5%) [28]. A comparison of the ^{37}Ar/^{36}Ar ratios measured by AMS and LLC is illustrated in Fig. 2.

Accelerator mass spectrometry of ^{39}Ar has been previously performed at ATLAS [33,34]. A high ion energy is essential for the separation and discrimination of ^{39}Ar from the extremely intense source background of the stable ^{39}K isobar. In our experiment, the ECR was operated at low power to reduce as much as possible impinging of the plasma onto the chamber walls, believed to be a source of ^{39}K contamination. ^{38,39,40}Ar^{8+} ions were accelerated to 6 MeV/u, similar to previously described and ^{39}Ar^{8+} ions were analyzed in the Enge gas-filled magnetic spectrograph [35], which physically separates ^{39}Ar from beam contaminants, e.g., ^{39}K^{8+} and ^{34}S^{7+}, which have close-by m/q values (Fig. 3). The accelerator transmission efficiency for ^{39}Ar^{8+} [0.40(3)] was interpolated between those of ^{38}Ar^{8+} and ^{40}Ar^{8+} [28].

The ratios $r = {}^{A+1}\mathrm{Ar}/{}^{A}\mathrm{Ar}$ at the end of irradiation are determined by $r = (N_{A+1}/\epsilon t)(qe/10^{-9} i_A) e^{\lambda t_{\mathrm{cool}}}$, where N_{A+1} is the number of $^{A+1}$Ar detected, ϵ is the detector efficiency [measured to be 0.91(3) for ^{38}Ar due to grid shadowing in the spectrograph focal-plane detector], t is the counting time, q is the ion charge state (18 for ^{37}Ar and 8 for ^{39}Ar), e is the electronic charge in coulomb, and i_A is the ^{A}Ar^{q+} beam intensity (nanoampere); $\lambda = (\ln(2)/t_{1/2})$ is the $^{A+1}$Ar decay constant and t_{cool} is the time between the end of irradiation and counting. The final results of the $^{A+1}$Ar/^{A}Ar ratios for all gas samples are presented in Table I.

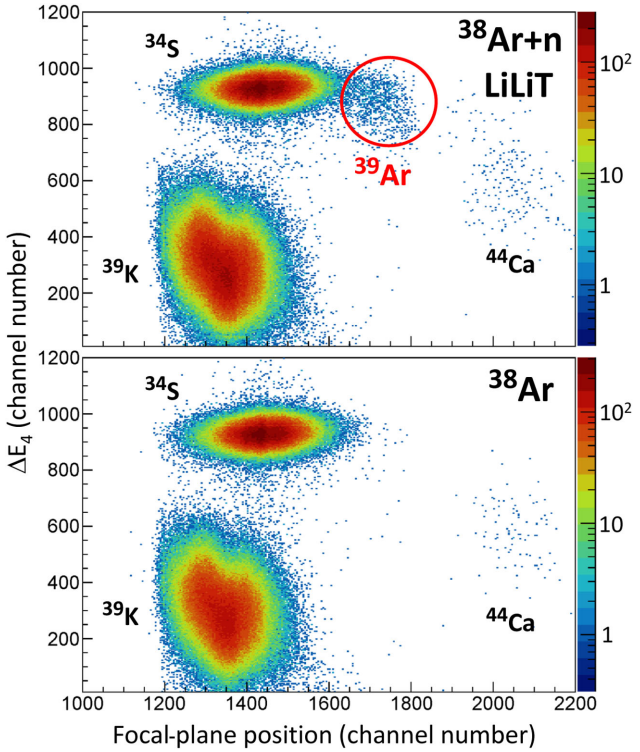

FIG. 3. Identification spectrum of ^{39}Ar ions in the detector measured for the LiLiT irradiated ^{38}Ar gas (top) and for non-irradiated ^{38}Ar gas (bottom). The horizontal axis represents dispersion along the focal plane and the vertical axis represents a differential energy loss signal measured in the fourth anode of the focal-plane ionization chamber [36].

In the reactor irradiations, two small Au samples were attached to the ^{36}Ar and ^{38}Ar spheres for neutron monitoring, using 98.65(9) b [37] for the ^{197}Au thermal neutron-capture cross section. A minor correction for the epithermal activation of Au was applied, using the ^{198}Au activity measured for a gas sphere entirely shielded with 1 mm thick Cd. In contrast to the ^{36}Ar sample, two ^{38}Ar samples irradiated at the reactor (Table I) were mixed with $^{\mathrm{nat}}$Ar to use ^{41}Ar ($\sigma_{\mathrm{th}}(^{40}\mathrm{Ar}) = 0.66(1)$ b [37]) as an internal neutron monitor in addition to the Au monitors; excellent agreement was obtained between the two neutron fluence calibrations [28]. The ^{36,38}Ar measured thermal-capture cross sections are listed in Table II. Uncertainties (1σ) for ^{36}Ar (^{38}Ar) are 3% (2%) and 7% (11%) from the neutron fluence and atom ratio determinations, respectively.

For the LiLiT irradiated samples, the average experimental cross section σ_{exp} is obtained by $\sigma_{\mathrm{exp}} = (r/\Phi_n)$, where Φ_n is the effective neutron fluence (n/cm^2). In view of the complex geometry of the gas sphere irradiation, Φ_n is calculated as $\Phi_n = (\sum l_n/V)$ where V (0.46 cm^3) is the gas sphere's volume, l_n is the length a neutron travels inside

the Ar gas, and $\sum l_n$ is the sum of the lengths traveled by all the neutrons inside the Ar gas sphere during the irradiation. $\sum l_n$ is calculated by a detailed simulation (see below), taking a statistically representative sample of neutrons and scaling by the Au activity. The validity of the expression $(\sum l_n/V)$ for the neutron fluence Φ_n was confirmed by comparing the value calculated in this way for the Au (planar) monitor with its measured activity; experimental and calculated values agree within 0.5%. The values of Φ_n (n/cm^2) and σ_{exp} for ^{36}Ar (^{38}Ar) are $6.2(1)\times10^{14}$ [$4.22(9)\times10^{14}$] and 1.4(1) mb [0.95(10) mb], respectively. Uncertainties (1σ) for the ^{36}Ar (^{38}Ar) experimental cross section σ_{exp} are 2% (2%) and 7% (11%) from the neutron fluence and atom ratio determinations, respectively.

The experimental cross section measured in our experiments is an energy-averaged value over the neutron spectrum and interpretation in terms of a Maxwellian averaged cross section (MACS) requires knowledge of the shape of the spectrum. The integral neutron spectrum seen by the targets under the irradiation conditions of the experiment is, however, not measurable. Instead, we rely on detailed simulations using the codes SimLiT [50] for the thick-target ^{7}Li(p,n) neutron yield and GEANT4 [51] for neutron transport (Fig. 1) [52]. The SimLiT-GEANT4 simulations have been carefully benchmarked in separate experiments and excellent agreement with experimental time of flight and (differential and integral) energy spectra was obtained [50,52,53]. The simulated neutron spectrum, $\frac{dn_{\mathrm{sim}}}{dE_n}$ is well fitted in the range $E_n\sim0$–110 keV (~90% of the incident neutrons) by a Maxwell-Boltzmann (MB) flux $v(dn_{\mathrm{MB}}/dE_n)\propto E_n\exp(-E_n/kT)$ with $kT\sim47$ keV (Fig. 1). The quantitative normalization of the neutron spectrum, (dn_{sim}/dE_n), was obtained by comparing the experimental number of ^{198}Au nuclei (measured by gamma activity with a high-purity germanium detector) in the Au foil monitor with the number of ^{198}Au nuclei calculated in the detailed simulation of the entire setup (see [52] for details).

We calculate the MACS at a given thermal energy kT with the procedure developed in [52,54], using the expression $\mathrm{MACS}(kT)=(2/\sqrt{\pi})C_{\mathrm{H\text{-}F}}(kT)\sigma_{\mathrm{exp}}$, where the correction factor $C_{\mathrm{H\text{-}F}}(kT)$ is given by

$$C_{\mathrm{H\text{-}F}}(kT)=\frac{\int_0^\infty\sigma(E_n)E_ne^{-\frac{E_n}{kT}}dE_n}{\int_0^\infty E_ne^{-\frac{E_n}{kT}}dE_n}\Bigg/\frac{\int_0^\infty\sigma(E_n)\frac{dn_{\mathrm{sim}}}{dE_n}dE_n}{\int_0^\infty\frac{dn_{\mathrm{sim}}}{dE_n}dE_n}. \quad (1)$$

$\sigma(E_n)$ may have coherent contributions from compound resonances and (weakly energy-dependent) direct captures (DC). We note here that σ_{exp} includes all contributions in the experimental energy range; we use in Eq. (1) the Hauser-Feshbach model for the energy dependence of $\sigma(E_n)$ in the wider MB range and estimate the additional uncertainties associated with direct capture. In order to account for the sensitivity to the low density of available compound states in ^{37,39}Ar, we apply different codes [28]: TENDL-2014 [55], -2015 [48], -2017 [56], and TALYS-1.8 [57] with a microscopic level density and average the $C_{\mathrm{H\text{-}F}}(kT)$ values obtained; the greater of 20% of the correction or their standard deviation is attributed to the MACS corrections. It should, however, be noted that the extrapolation of the MACS to different thermal energies and determination of their uncertainties were made using a limited number of theoretical models, due to the total absence of experimental knowledge of resonances in the ^{37,39}Ar compound nuclei. We also add an estimated independent 15% uncertainty from s- and p-wave DC contributions. Detailed calculations of the correction factor and its uncertainties will be included in an expanded version of this Letter. Our MACS values and uncertainties are listed in Table II and compared to existing theoretical values.

TABLE II. Comparison of the experimental thermal cross sections and MACS (30 keV) obtained in this Letter to theoretical and evaluated data.

Year [Ref.]	^{36}Ar	^{38}Ar
	Thermal cross section (b)	
1950 [38]	6.5(10)	
1968 [39]	5.0(8)	
1952 [40]		0.8(2)
2006 [37]	5.2(5)	0.8(2)
This Letter	3.9(3)	0.68(8)
	MACS (30 keV) (mb)	
1978 [41]	6.7	2.6
1983 [42]	8	
2000 [43]	14	3.9
2005 [44]	24.6	8.07
2011 [45–47]	8.86	0.137
2015 [48]	8.48	2.82
Kadonis [49]	9.0(15)	3.0(3)
This Letter (30 keV)	1.9(3)	1.3(2)
This Letter (47 keV)	1.4(2)	0.92(16)

The experimental MACS values (Table II) obtained in this Letter are notably different from previous calculations. Figure 4 shows the ^{36,38}Ar(n,γ) reaction rates $(N_A\langle\sigma v\rangle)$ based on our measurements and extrapolation to different temperatures, compared to the rates adopted so far [49]. In order to show the potential effect of these experimental rates on stellar nucleosynthesis, we performed a single-zone network calculation using physical conditions appropriate for the He-core-burning phase of a massive star, in which the new ^{36,38}Ar(n,γ) rates were used, leaving all others unchanged [49]. The calculations were done using the single-zone NucNet Tools reaction network code [58] starting at the H-burning phase with solar abundances [3] and continuing into a single-zone He core burning ($T=300$ MK, density of 1 kg/cm^3). Substantial (10%–50%) changes in the calculated mass fractions for neutron-rich light nuclides between ^{34}S and ^{58}Fe are observed

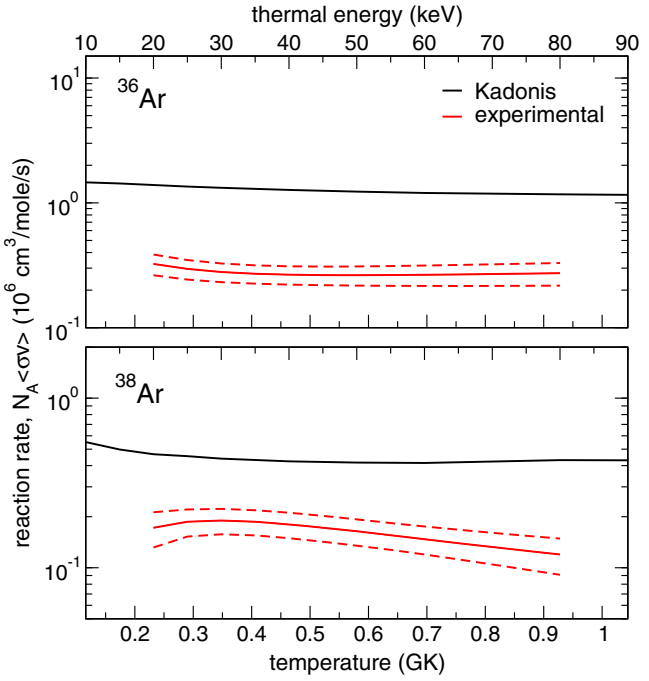

FIG. 4. Comparison of the ^{36}Ar (top) and ^{38}Ar (bottom) (n,γ) reaction rates ($N_A\langle\sigma v\rangle$) extracted from this Letter (red) to the Kadonis [49] recommended values (black). The dashed curves encompass the estimated 1σ uncertainty.

(Fig. 5), reminiscent of the sensitivity observed in the weak s-process region ($A \sim 56$–70) due to the change of a single cross section [59]. The mass fraction of ^{36}Ar itself is observed to increase by a factor of $\sim$10 due to its lower

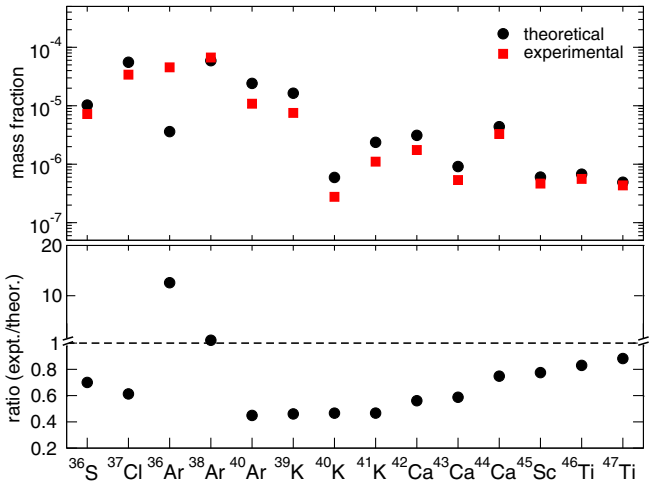

FIG. 5. (Top) Comparison of the mass fractions calculated for stable nuclei between ^{34}S and ^{58}Fe changing by $>10\%$ at the end of a single-zone calculation modeling He burning in a massive star, using literature rates [49] (solid circles) or replacing the ^{36,38}Ar(n,γ) rates with the experimental values from this Letter (solid squares). We observe a smoother distribution of mass fractions in the vicinity of ^{36}Ar when using the experimental cross sections. (Bottom) Ratio of the mass fractions using experimental and literature reaction rates as above.

measured capture-cross section. Especially interesting is the $\sim$45% decrease in the calculated mass fraction of the important cosmo- or geochronometer ^{40}K, implying a weaker contribution of the secondary s process relative to primary production. As shown in Frank *et al.* [60], the mass fraction of ^{40}K differs considerably over time, whether it is primary only or secondary only. For example, with a larger primary production of ^{40}K, which is the dominant initial heat generator in Earth-like exoplanets, considerable heating would occur in these worlds even early in the Galaxy history.

The measurements of the ^{36}Ar(n,γ) cross sections affect also the calculation of the natural ^{37}Ar background activity in the atmosphere, the interpretation of ^{37}Ar emission rates in underground nuclear explosion monitoring [16], and the investigation of atmospheric air circulation [11]. The detection of ^{37}Ar by AMS demonstrated here opens the way to an alternative method for the monitoring of environmental samples [22]. Similar to ^{37}Ar, the ^{38}Ar$(n,\gamma)^{39}$Ar reaction contributes to the ^{39}Ar production rate in the atmosphere [11] and determines the initial value for the use of ^{39}Ar as a groundwater dating chronometer [13,14,61].

In summary, first measurements of the neutron-capture cross sections of ^{36}Ar and ^{38}Ar at stellar energies were performed. The experimental value for ^{36}Ar, in particular, is smaller than the one adopted so far from theoretical calculations and evaluations by a factor of $\sim$10. Nucleosynthesis calculations for the weak s-process regime using the measured cross sections are shown to increase the mass fraction of ^{36}Ar by a factor of $\sim$10 and lower the residual mass fraction of neutron-rich nuclides in the region $A = 36$–48 by 10%–50%. The ^{36,38}Ar(n,γ) cross sections affect the interpretation of environmental monitoring using ^{37}Ar or ^{39}Ar as geophysical tracers.

We would like to thank the SARAF and LiLiT (Soreq NRC) and the ATLAS operation staffs for their dedicated help during the experiments. This work was supported in part by the Israel Science Foundation (Grant No. 1387/15), by the Pazy Foundation (Israel), the Israel Ministry of Science (Eshkol Grant No. 18145), the U.S. Department of Energy, Office of Nuclear Physics, under Award No. DE-AC02-06CH11357. D. S. G. acknowledges the support by the U.S. Department of Energy, Office of Nuclear Physics, under Award No. DE-FG02-96ER40978. This research has received funding from the European Research Council under the European Union's Seventh Framework Program (FP/2007-2013)/ERC Grant Agreement No. 615126.

*Corresponding author.
paul@vms.huji.ac.il

[1] C. F. von Weizsäcker, The possibility of a dual β-decomposition in potassium, Phys. Z. **38**, 623 (1937).
[2] E. Anders and T. Owen, Mars and Earth: origin and abundance of volatiles, Science **198**, 453 (1977).

[3] K. Lodders, Solar system abundances and condensation temperatures of the elements, Astrophys. J. **591**, 1220 (2003).

[4] R. D. Hoffman, S. E. Woosley, T. A. Weaver, T. Rauscher, and F.-K. Thielemann, The reaction rate sensitivity of nucleosynthesis in type II supernovae, Astrophys. J. **521**, 735 (1999).

[5] R. Reifarth, K. Schwarz, and F. Käppeler, The stellar neutron-capture rate of ^{34}S: the origin of ^{36}S challenged, Astrophys. J. **528**, 573 (2000).

[6] J. Chen, Nuclear data sheets for $A = 40$, Nucl. Data Sheets **140**, 1 (2017).

[7] E. M. Burbidge, G. R. Burbidge, W. A. Fowler, and F. Hoyle, Synthesis of the elements in stars, Rev. Mod. Phys. **29**, 547 (1957).

[8] H. Beer and R.-D. Penzhorn, Measurement of the neutron capture cross section of Ar-40 and an *s*-process analysis from S-34 to Ca-42, Astron. Astrophys. **174**, 323 (1987).

[9] D. D. Clayton, , *Handbook of the Isotopes in the Cosmos* (Cambridge University Press, Cambridge, England, 2003).

[10] J. Cameron, J. Chen, B. Singh, and N. Nica, Nuclear data sheets for $A = 37$, Nucl. Data Sheets **113**, 365 (2012).

[11] H. H. Loosli, H. Oeschger, and W. Wiest, Argon 37, argon 39, and krypton 81 in the atmosphere and tracer studies based on these isotopes, J. Geophys. Res. **75**, 2895 (1970).

[12] B. Singh and J. A. Cameron, Nuclear data sheets for $A = 39$, Nucl. Data Sheets **107**, 225 (2006).

[13] J. A. Corcho Alvarado, R. Purtschert, F. Barbecot, C. Chabault, J. Rueedi, V. Schneider, W. Aeschbach-Hertig, R. Kipfer, and H. H. Loosli, Constraining the age distribution of highly mixed groundwater using ^{39}Ar: A multiple environmental tracer (^{3}H/^{3}He, ^{85}Kr, ^{39}Ar, and ^{14}C) study in the semiconfined Fontainebleau Sands Aquifer (France), Water Resour. Res. **43**, W03427 (2007).

[14] H. H. Loosli, A dating method with ^{39}Ar, Earth Planet. Sci. Lett. **63**, 51 (1983).

[15] P. Schlosser, B. Kromer, G. Östlund, B. Ekwurzel, G. Bönisch, H. H. Loosli, and R. Purtschert, On the ^{14}C and ^{39}Ar distribution in the central arctic ocean: Implications for deep water formation, Radiocarbon **36**, 327 (1994).

[16] R. Riedmann and R. Purtschert, Natural ^{37}Ar concentrations in soil air: implications for monitoring underground nuclear explosions, Environ. Sci. Technol. **45**, 8656 (2011).

[17] A. Kreisel *et al.*, Phase-I proton/deuteron linac beam operation status, in *Proceedings of Linac 2014, Geneva (Switzerland)*, (WEIOB02 770, 2014), and references therein, http://accelconf.web.cern.ch/AccelConf/LINAC2014/papers/weiob02.pdf.

[18] I. Mardor *et al.*, The Soreq Applied Research Accelerator Facility (SARAF): overview, research programs and future plans, Eur. Phys. J. A **54**, 91 (2018).

[19] S. Halfon *et al.*, High-power liquid-lithium jet target for neutron production, Rev. Sci. Instrum. **84**, 123507 (2013).

[20] S. Halfon *et al.*, Note: Proton irradiation at kilowatt-power and neutron production from a free-surface liquid-lithium target, Rev. Sci. Instrum. **85**, 056105 (2014).

[21] M. Paul *et al.*, Nucleosynthesis reactions with the high-intensity SARAF-LiLiT neutron source, Proc. Sci., INPC2016 (**2017**) 139; https://pos.sissa.it/281/139/pdf.

[22] M. Paul *et al.*, Positive-ion accelerator mass spectrometry at ATLAS: peaks and pits, in *Proceedings of The Fourteenth International AMS Conference (AMS14), 2017, Ottawa (Canada)* (to be published).

[23] G. Rupp, D. Petrich, F. Käppeler, J. Kaltenbaek, B. Leugers, and R. Reifarth, High pressure gas spheres for neutron and photon experiments, Nucl. Instrum. Methods Phys. Res., Sect. A **608**, 152 (2009).

[24] G. Feinberg, Study of the $^7\mathrm{Li}(p,n)$ Reaction Towards Measurements of Neutron-Capture Cross Sections in the Astrophysical *s*-process With the SARAF Accelerator and a Liquid-Lithium Target, Ph.D. thesis, Hebrew University, 2014 (unpublished); http://arad.mscc.huji.ac.il/dissertations/W/JSL/001975970.pdf.

[25] M. Paul *et al.*, First nuclear-astrophysics experiments with high-intensity neutrons form the liquid-lithium target LiLiT, Proc. Sci. NIC, XIII2014 (**2014**) 059.

[26] Model PFC16A, Centronics, Ltd., UK; http://www.centronic.co.uk/.

[27] Trace Sciences International Corporation, http://www.tracesciences.com/.

[28] See Supplemental Material at http://link.aps.org/supplemental/10.1103/PhysRevLett.121.112701 for additional information.

[29] R. Davis, A review of the homestake solar neutrino experiment, Prog. Part. Nucl. Phys. **32**, 13 (1994).

[30] H. H. Loosli, M. Möll, H. Oeschger, and U. Schotterer, Ten years low-level counting in the underground laboratory in Bern, Switzerland, Nucl. Instrum. Methods Phys. Res., Sect. B **17**, 402 (1986).

[31] J. P. Renier, H. Genz, K. W. D. Ledingham, and R. W. Fink, $\frac{M}{L}$ orbital-electron-capture ratio in Ar^{37} decay and the fraction of K_α X rays in the K series of chlorine, Phys. Rev. **166**, 935 (1968).

[32] Thermo Finnigan MAT 253, Thermo Electron Corporation; http://www.thermo.com.

[33] P. Collon *et al.*, Development of an AMS method to study oceanic circulation characteristics using cosmogenic ^{39}Ar, Nucl. Instrum. Methods Phys. Res., Sect. B **223**, 428 (2004).

[34] P. Collon *et al.*, Reducing potassium contamination for AMS detection of ^{39}Ar with an electron-cyclotron-resonance ion source, Nucl. Instrum. Methods Phys. Res., Sect. B **283**, 77 (2012).

[35] M. Paul, B. G. Glagola, W. Henning, J. G. Keller, W. Kutschera, Z. Liu, K. E. Rehm, B. Schneck, and R. H. Siemssen, Heavy ion separation with a gas-filled magnetic spectrograph, Nucl. Instrum. Methods Phys. Res., Sect. A **277**, 418 (1989).

[36] M. Paul *et al.*, A new large area focal plane detector for the ATLAS split pole spectrograph, Argonne National Laboratory, Argonne, Illinois, USA, Physics Division Annual Report No. ANL-97/14, 1997, p. 79, https://inldigitallibrary.inl.gov/Reports/ANL-97-14.pdf.

[37] S. F. Mughabghab, *Atlas of Neutron Resonances* (Elsevier Science, New York, 2006).

[38] G. E. McMurtrie and D. P. Crawford, The thermal neutron-capture cross section of A^{36}, Phys. Rev. **77**, 840 (1950).

[39] P. Wille, The decay of ^{37}Ar following neutron capture in ^{36}Ar, Atomkernenergie **13**, 383 (1968).

[40] S. Katcoff, Thermal neutron capture cross section of A^{40} and observation of A^{42}, Phys. Rev. **87**, 886 (1952).
[41] S. Woosley, W. A. Fowler, J. A. Holmes, and B. A. Zimmerman, Semiempirical thermonuclear reaction-rate data for intermediate-mass nuclei, At. Data Nucl. Data Tables **22**, 371 (1978).
[42] H. Gruppelaar and H. van der Kamp, Evaluation of activation cross sections of corrosion products, cover-glass nuclides and other nuclides in the primary cooling circuit of a fast power reactor, *Nuclear Data for Science and Technology*, edited by K. Böckhoff (D. Reidel Publishing Company, Dordrecht, Holland, 1983), p. 643.
[43] T. Rauscher and F.-K. Thielemann, Astrophysical reaction rates from statistical model calculations, At. Data Nucl. Data Tables **75**, 1 (2000).
[44] S. Goriely, Hauser-Feshbach rates for neutron-capture reactions, Ver. 8/29/2005, http://www-astro.ulb.ac.be/Html/hfr.html.
[45] M. B. Chadwick *et al.*, ENDF/B-VII.1 nuclear data for science and technology: cross sections, covariances, fission product yields and decay data, Nucl. Data Sheets **112**, 2887 (2011).
[46] JEFF-3.2 Library, Joint Evaluated Fission and Fusion (2014), https://www.oecd-nea.org/dbforms/data/eva/evatapes/jeff_32/.
[47] ROSFOND-2010 Library, Institute of Physics and Power Engineering (2010), http://www.ippe.ru/podr/abbn/libr/rosfond.php.
[48] A. J. Koning *et al.*, TENDL-2015, https://tendl.web.psi.ch/tendl_2015/tendl2015.html.
[49] I. Dillmann *et al.*, KADoNiS—The Karlsruhe Astrophysical Database of Nucleosynthesis in Stars, AIP Conf. Proc. **819**, 123 (2006).
[50] M. Friedman *et al.*, Simulation of the neutron spectrum from the $^{7}\mathrm{Li}(p,n)$ reaction with a liquid-lithium target at Soreq Applied Research Accelerator Facility, Nucl. Instrum. Methods Phys. Res., Sect. A **698**, 117 (2013).
[51] S. Agostinelli *et al.*, Geant4—a simulation toolkit, Nucl. Instrum. Methods Phys. Res., Sect. A **506**, 250 (2003).
[52] M. Tessler *et al.*, Stellar 30-keV neutron capture in ^{94,96}Zr and the $^{90}\mathrm{Zr}(\gamma,n)^{89}$Zr photonuclear reaction with a high-power liquid-lithium target, Phys. Lett. B **751**, 418 (2015).
[53] G. Feinberg *et al.*, Quasi-stellar neutrons from the $^{7}\mathrm{Li}(p,n)^{7}$Be reaction with an energy-broadened proton beam, Phys. Rev. C **85**, 055810 (2012).
[54] M. Tessler *et al.*, Stellar 30-keV neutron capture in ^{94,96}Zr and the $^{90}\mathrm{Zr}(\gamma,n)^{89}$Zr photonuclear reaction with a high-power liquid-lithium target, Supp. Mat., Phys. Lett. B **751**, 418 (2015); https://ars.els-cdn.com/content/image/1-s2.0-S0370269315008175-mmc1.pdf.
[55] A. J. Koning and D. Rochman, Modern nuclear data evaluation with the TALYS code system, Nucl. Data Sheets **113a**, 2841 (2012).
[56] A. J. Koning *et al.*, TENDL-2017, https://tendl.web.psi.ch/tendl_2017/tendl2017.html.
[57] A. Koning, S. Hilaire, and S. Goriely, TALYS-1.8, NRG-1755 ZG Petten, The Netherlands (2015), http://www.talys.eu/home/.
[58] https://sourceforge.net/projects/nucnet-tools/.
[59] H. Nassar *et al.*, Stellar (n,γ) Cross Section of ^{62}Ni, Phys. Rev. Lett. **94**, 092504 (2005).
[60] E. A. Frank, B. S. Meyer, and S. J. Mojzsis, A radiogenic heating evolution model for cosmochemically Earth-like exoplanets, Icarus **243**, 274 (2014).
[61] P. Collon, W. Kutschera, and Z. T. Lu, Tracing noble gas radionuclides in the environment, Annu. Rev. Nucl. Part. Sci. **54**, 39 (2004).